J. Fluid Mech. (2013), *vol.* 723, *pp.* 140–162. © Cambridge University Press 2013
doi:10.1017/jfm.2013.127

Lagrangian approach to laminar–turbulent interfaces in transitional pipe flow

Markus Holzner[1],†, Baofang Song[1], Marc Avila[1,2] and Björn Hof[1]

[1]Max Planck Institute for Dynamics and Self-Organisation, Bunsenstraße 10, 37073 Göttingen, Germany

[2]Institute of Fluid Mechanics, Friedrich-Alexander-Universität Erlangen-Nürnberg, Cauerstraße 4, 91058 Erlangen, Germany

(Received 6 June 2012; revised 10 January 2013; accepted 25 February 2013; first published online 16 April 2013)

Transition in shear flows is characterized by localized turbulent regions embedded in the surrounding laminar flow. These so-called turbulent spots or puffs are observed in a variety of shear flows and in certain Reynolds-number regimes, and they are advected by the flow while keeping their characteristic length. We show here for the case of pipe flow that this seemingly passive advection of turbulent puffs involves continuous entrainment and relaminarization of laminar and turbulent fluid across strongly convoluted interfaces. Surprisingly, interface areas are almost two orders of magnitude larger than the pipe cross-section, while local entrainment velocities are much smaller than the mean speed. Even though these velocities were shown to be small and proportional to the Kolmogorov velocity scale (in agreement with a prediction by Corrsin) in a flow without mean shear before, we find that, in pipe flow, local entrainment velocities are about an order of magnitude smaller than this scale. The Lagrangian method used to study the dynamics of the laminar–turbulent interfaces allows accurate determination of the leading and trailing edge speeds. However, to resolve the highly complex interface dynamics requires much higher numerical resolutions than for ordinary turbulent flows. This method also reveals that the volume flux across the leading edge has the same radial dependence but the opposite sign as that across the trailing edge, and it is this symmetry that is responsible for the puff shape remaining constant.

Key words: instability, pattern formation, transition to turbulence

1. Introduction

Perhaps the earliest works that focus specifically on the interface between laminar and turbulent flow regions in pipes are the investigations of Rotta (1956) and Lindgren (1969). Using simple momentum and energy balance considerations over a control volume moving with the interface, Rotta (1956) predicted that the spreading speed of leading and trailing edges of localized turbulence is comparable to the flow rate. A similar analysis was carried out by Lindgren (1969) and the predicted spreading speeds were compared to experimental data.

† Email address for correspondence: holzner@ifu.baug.ethz.ch

https://doi.org/10.1017/jfm.2013.127 Published online by Cambridge University Press

In two seminal papers, Wygnanski and coworkers (Wygnanski & Champagne 1973; Wygnanski, Sokolov & Friedman 1975) described that, at low Reynolds numbers $Re \simeq 2200$, the flow regime in transitional pipe flow consists of localized turbulent structures called *puffs* bounded by regions of laminar flow ($Re := UD/\nu$, where U is the mean flow velocity, D is the diameter of the pipe and ν is the kinematic viscosity of the fluid). Puffs are characterized by a steep laminar–turbulent interface at the trailing edge and a more diffused leading edge, and maintain an average length of about 20 pipe diameters. More recently, it was found that puffs are not sustained but transient, i.e. they relaminarize after very long but finite times after their generation (Hof *et al.* 2006, 2008; Avila, Willis & Hof 2010). At higher Reynolds number $Re \simeq 3000$, localized turbulence becomes more vigorous, with steep interfaces at both the leading and trailing edges; these structures were called *slugs* (Wygnanski & Champagne 1973). In contrast to puffs, slugs were observed to grow continuously in size over time with considerable speed. It is worth noting that puffs can also spread and contaminate laminar flow by splitting, a process by which a puff first grows in size and then splits into two through the formation of a laminar gap in between (Wygnanski & Champagne 1973; Moxey & Barkley 2010). Indeed it is the balance between spreading and relaminarization of puffs that sets the critical Reynolds number $Re_c = 2040$ for the onset of self-sustained turbulence in pipes (Avila *et al.* 2011). As Re is increased beyond 2040, the probability of a puff to split surpasses the decay probability. Hence for $Re > 2040$ the number of puffs and therefore the turbulent fraction in pipes on average increases (strictly, as is the case for any phase transition, the critical point is only assumed in the thermodynamic limit). As also pointed out in Avila *et al.* (2011), the time scale for splitting as well as that for decay are extremely large, and both processes are memoryless. The latter infers that puffs do not age. They travel downstream at a constant size (i.e. the size statistically fluctuates around a mean value) for very long times until they abruptly decay or split. For example, at $Re = 2200$, the median time to split is still $\sim 10^4 D/U$.

Based on a conditional analysis in coordinates moving with the laminar–turbulent interface, Wygnanski & Champagne (1973) found that slugs entrain laminar fluid at both the trailing and leading edges. Relaminarization of fluid seemed to be prevented, though fluid possibly leaves the slug through the viscous sublayer close to the wall (Wygnanski & Champagne 1973). Their analysis of the energy budget near the interfaces showed that gradient diffusion (including pressure diffusion) may be responsible for entrainment of laminar fluid. On average, production of kinetic energy was also significant at the interface, whereas viscous dissipation was important only in the interior of the slug. Based on these results Wygnanski & Champagne (1973) suggested the following dynamical picture (see also Townsend 1966). At the slug interfaces, large-scale eddies are formed, extracting energy from the mean shear. As fluid is entrained, turbulence intensities increase at the interface. While the larger eddies move towards the interior, they are quenched with the energy cascading towards smaller scales, where viscous dissipation occurs. At this point the turbulence intensity is low, allowing for the re-formation of the large-scale motion and the cycle starts over again.

Wygnanski *et al.* (1975) argued that puffs are qualitatively different from slugs, for example, in that they do not show a well-defined leading edge. As a possible explanation they inferred that local transition to turbulence, in which random vorticity is produced, occurs abruptly only through the trailing edge of the puff. The leading edge is purely characterized by relaminarization, a process in which vortices are aligned, stretched and finally dissipated while the mean flow accelerates. This process

https://doi.org/10.1017/jfm.2013.127 Published online by Cambridge University Press

is assumed to be much slower and hence may not be demarcated by an abrupt interface (Wygnanski *et al.* 1975). These observations are consistent with extensive flow visualization studies of puffs by Bandyopadhyay (1986), which indicated that the laminar faster-moving fluid upstream is continuously entrained into the slower-moving turbulent region through the trailing edge. Wake-like three-dimensional vortices are shed near the wall at the trailing edge, while at the leading edge longitudinal vortices undergo stretching and decay slowly (Bandyopadhyay 1986).

Darbyshire & Mullin (1995) used a constant-mass flux pipe and conducted flow visualization and laser Doppler measurements in transitional pipe flow. Their interpretation of the measurements offered two scenarios for the maintenance of sharp interfaces and localized turbulence (Darbyshire & Mullin 1995). The first scenario is that the rear interface of a puff cyclically entrains the faster laminar fluid in the central region of the pipe. The excess energy of the faster-moving fluid is converted to turbulence production as the fluid is swept out towards the pipe wall. The second proposed scenario is that 'the interface is not a constant feature but breaks and remakes itself intermittently'. The turbulent flow region is moving at a speed of about U, while the laminar fluid in the central axis region has a greater speed of up to $2U$. The turbulent region can thus be considered as a barrier moving at lower speed and can only be overcome provided that enough momentum has built up in front of it. Again, the energy of the faster fluid would sustain the turbulence. Darbyshire & Mullin (1995) also inferred that, since slugs move at larger speed compared to puffs, one might expect the turbulence production to be greater for slugs so that the front interface moves at a speed higher than U. In that case entrainment might occur at both the trailing and leading interfaces (Darbyshire & Mullin 1995).

Direct numerical simulations by Shan *et al.* (1999) of a puff at $Re = 2200$ and a slug at $Re = 5000$ reproduced some of the features observed experimentally. In particular, the obtained profiles of the streamwise velocity and recirculation patterns showed qualitative similarity to measured data. The simulated puff structure was not in equilibrium but expanded, which was attributed to the small size of the simulation domain (Shan *et al.* 1999). Based on the analysis of trajectories of advected fluid particles, the authors concluded that puffs entrain fluid only through the leading edge and detrain it through the trailing edge (Shan *et al.* 1999), which seems at variance with previous literature.

Recently, van Doorne & Westerweel (2009) have conducted time-resolved stereoscopic particle image velocimetry (PIV) measurements over the cross-section of the pipe, revealing the quasi-instantaneous velocity field of a puff. Consistent with the visualizations of Bandyopadhyay (1986), they showed that transition to turbulence at the trailing edge is associated with the quasi-periodic regeneration of counter-rotating streamwise vortices, which might be the legs of so-called hairpin vortices that develop and become stronger in the turbulent region of the puff. It was proposed that, since the axial velocity profile is relatively flat in the core of the puff, these structures may not be able to extract enough energy from the shear to be sustained and decay (van Doorne & Westerweel 2009). Further downstream, as the flow relaminarizes, the kinetic energy increases and strong shear layers develop again, so that a new puff may be created via splitting.

Shimizu & Kida (2009) used direct numerical simulations (DNSs) of a turbulent puff in pipe flow at $Re = 2226$. As a driving mechanism for the puff, they identified strong vortex layers that form at the trailing edge, presumably through Kelvin–Helmholtz instabilities of low-speed streaks. The streaks, originally generated in the turbulent region through near-wall interactions, are slower than the puff and

https://doi.org/10.1017/jfm.2013.127 Published online by Cambridge University Press

penetrate the trailing edge. The roll-up of the vortex layers energizes the turbulence activity in the puff via velocity fluctuations that propagate downstream faster than the puff (Shimizu & Kida 2009). Similarly, Hof *et al.* (2010) proposed that turbulent puffs are sustained by an inflection point instability, where streamwise vortices distort the velocity profile by shuffling low-speed fluid towards the centre. Vortices mostly roll up at the upstream interface, where the inflection point is located and the vorticity magnitude is highest, and progress downstream with the mean flow. These insights have then been exploited to suppress turbulence via control strategies (Hof *et al.* 2010).

At this point it is important to remark that the main findings up to now are consistent with the entrainment hypothesis put forward by Townsend (1966), who suggested that at the laminar–turbulent interface the rate of entrainment of laminar fluid is controlled by larger-scale eddies that draw their energy from the mean flow and contort and increase the interface area across which small-scale transfer of vorticity can take place. The transfer of vorticity is supposedly a viscous process (Corrsin & Kistler 1955), when the non-turbulent flow is irrotational. Measurements in developing turbulence without mean shear give evidence that this is indeed the case (Holzner *et al.* 2008; Holzner & Lüthi 2011) and are corroborated by recent experiments at the boundary of a round jet (Wolf *et al.* 2012). In pipe flow, however, the average laminar turbulence interface is essentially normal to the mean motion, and some time ago Corrsin & Kistler (1955) noted that the turbulence may propagate differently in this case: indeed, *a destabilization of the already rotational flow might take place* in addition to the viscous diffusion of fluctuating vorticity.

Holzner & Lüthi (2011) recently presented a quantitative approach that enables one to calculate the interface propagation velocity and to disentangle the different mechanisms at work. The approach is essentially Lagrangian and separates between advection by the fluid velocity and velocity relative to the fluid. It is based on the fact that the local propagation velocity v_n of an enstrophy isosurface relative to the fluid is given by the ratio between the material derivative $\mathrm{D}\omega^2/\mathrm{D}t$ and the magnitude of the gradient $|\nabla\omega^2|$, as $v_n = -(\mathrm{D}\omega^2/\mathrm{D}t)/|\nabla\omega^2|$ (Holzner & Lüthi 2011), where $\omega^2 = \boldsymbol{\omega}\cdot\boldsymbol{\omega}$ is the enstrophy ($\boldsymbol{\omega} = \nabla\times\boldsymbol{u}$ is the fluctuating vorticity vector and $\boldsymbol{u}$ is the fluctuating flow velocity). For example, fluid regions where $v_n < 0$ are entrained into the turbulent region, whereas flow regions where $v_n > 0$ relaminarize. The approach hence allows one to study where and how transition to turbulence occurs locally. In this paper we extend the approach to localized turbulence in pipe flow, as proposed in Holzner *et al.* (2011). The paper is organized as follows. In § 2 we explain the method, whereas the numerical implementation is discussed in § 3. The results are shown in § 4, with a discussion in § 5 and, finally, we draw the conclusions in § 6.

2. Lagrangian method to compute interface propagation velocity

We consider the motion of incompressible fluid driven through a circular pipe with a fixed mass flux. Normalizing lengths by $D/2$ and velocities by $2U$, the Navier–Stokes equations read

$$\partial_t\tilde{\boldsymbol{u}} + (\tilde{\boldsymbol{u}}\cdot\nabla)\tilde{\boldsymbol{u}} = -\nabla\tilde{p} + \frac{1}{Re}\Delta\tilde{\boldsymbol{u}}. \tag{2.1}$$

Cylindrical coordinates (r,θ,z) are employed in the numerical solution, with no-slip boundary conditions at the pipe wall $r = 1$ and periodicity imposed on the azimuthal θ and axial z directions. The laminar velocity $\boldsymbol{U} = (1-r^2)\boldsymbol{e}_z$ is used to decompose

https://doi.org/10.1017/jfm.2013.127 Published online by Cambridge University Press

the velocity field as $\tilde{\boldsymbol{u}} = \boldsymbol{u} + \boldsymbol{U}$, where $\boldsymbol{u}$ is the perturbation velocity field. Herein lower-case letters with ˜ denote total quantities, lower-case ones without ˜ denote deviations from the basic laminar flow and capital letters denote quantities of laminar flow. For example, the vorticity of the perturbation velocity field is $\boldsymbol{\omega} = \boldsymbol{\nabla} \times \boldsymbol{u}$.

2.1. *Local propagation velocity relative to the fluid*

Holzner & Lüthi (2011) recently derived an expression for the propagation velocity of a laminar–turbulent interface in a flow without mean shear. However, note that, in pipe flow, the laminar velocity profile has non-zero shear. There is one non-zero derivative in the radial direction, where the vorticity is $\Omega_\theta = -\partial W/\partial r$ and the rate of strain is $S_{rz} = S_{zr} = \partial W/2\partial r$. In the following we extend the approach of Holzner & Lüthi (2011) to account for the laminar mean velocity profile in pipe flow and use cylindrical coordinates. As the interfaces at the edge of puffs and slugs are characterized by steep gradients of fluctuating vorticity magnitude (e.g. Wygnanski & Champagne 1973), a threshold or isolevel on the perturbation enstrophy is a suitable criterion to define the interface between laminar and turbulent flow.

In a Lagrangian frame moving with a patch of the iso-enstrophy surface, the isolevel will by definition remain constant and this can be used to derive an expression for the propagation velocity (Holzner & Lüthi 2011). We write the velocity of an isosurface element, $\boldsymbol{u}^s$, as the sum of the fluid velocity, $\tilde{\boldsymbol{u}}$, and the velocity of the area element relative to the fluid, $\boldsymbol{V} = v_n\hat{\boldsymbol{n}}$, that is, $\boldsymbol{u}^s = \tilde{\boldsymbol{u}} + \boldsymbol{V}$, where $\hat{\boldsymbol{n}} = \boldsymbol{\nabla}\omega^2/|\boldsymbol{\nabla}\omega^2|$ is the surface normal and v_n is the normal velocity component. The total change of ω^2 in the frame of reference moving with an enstrophy isosurface element is written as

$$\frac{\mathrm{D}^s\omega^2}{\mathrm{D}^s t} = \frac{\partial\omega^2}{\partial t} + \boldsymbol{u}^s \cdot \boldsymbol{\nabla}\omega^2 = \frac{\partial\omega^2}{\partial t} + (\tilde{\boldsymbol{u}} + \boldsymbol{V}) \cdot \boldsymbol{\nabla}\omega^2 = 0. \tag{2.2}$$

The isosurface will hence evolve according to the relation

$$\frac{\partial\omega^2}{\partial t} + \tilde{\boldsymbol{u}} \cdot \boldsymbol{\nabla}\omega^2 = \frac{\mathrm{D}^{\tilde{u}}\omega^2}{\mathrm{D}^{\tilde{u}} t} = -\boldsymbol{V} \cdot \boldsymbol{\nabla}\omega^2 = -v_n|\boldsymbol{\nabla}\omega^2| \tag{2.3}$$

and so we get

$$v_n = -\frac{\dfrac{\mathrm{D}^{\tilde{u}}\omega^2}{\mathrm{D}^{\tilde{u}} t}}{|\boldsymbol{\nabla}\omega^2|}. \tag{2.4}$$

2.2. *Components of the local propagation velocity and their physical origin*

We can use the vorticity transport equation and decompose the material change of enstrophy $\mathrm{D}^{\tilde{u}}\omega^2/\mathrm{D}^{\tilde{u}} t$ into different components. First, we express the term as $\mathrm{D}^{\tilde{u}}\omega^2/\mathrm{D}^{\tilde{u}} t = 2\omega_i \mathrm{D}^{\tilde{u}}\omega_i/\mathrm{D}^{\tilde{u}} t$ and focus on the vector $\mathrm{D}^{\tilde{u}}\omega_i/\mathrm{D}^{\tilde{u}} t$, written as follows:

$$\frac{\mathrm{D}^{\tilde{u}}\omega_i}{\mathrm{D}^{\tilde{u}} t} = \frac{\mathrm{D}^{\tilde{u}}(\tilde{\omega}_i - \Omega_i)}{\mathrm{D}^{\tilde{u}} t} = \frac{\mathrm{D}^{\tilde{u}}\tilde{\omega}_i}{\mathrm{D}^{\tilde{u}} t} - \frac{\mathrm{D}^{\tilde{u}}\Omega_i}{\mathrm{D}^{\tilde{u}} t}. \tag{2.5}$$

The second term on the right-hand side of (2.5) can be expressed as

$$\frac{\mathrm{D}^{\tilde{u}}\Omega_i}{\mathrm{D}^{\tilde{u}} t} = \frac{\partial\Omega_i}{\partial t} + (\tilde{\boldsymbol{u}} \cdot \boldsymbol{\nabla})\Omega_i, \tag{2.6}$$

where the only non-zero component is

$$\frac{\mathrm{D}^{\tilde{u}}\Omega_\theta}{\mathrm{D}^{\tilde{u}} t} = u\frac{\partial\Omega_\theta}{\partial r} - \frac{u\Omega_\theta}{r}. \tag{2.7}$$

https://doi.org/10.1017/jfm.2013.127 Published online by Cambridge University Press

Using the balance equation for the total vorticity vector, the first term on the right-hand side of (2.5) can be expressed as

$$\frac{\mathrm{D}^{\tilde{u}}\tilde{\omega}_i}{\mathrm{D}^{\tilde{u}}t} = \tilde{\omega}_j\tilde{s}_{ij} + \frac{1}{Re}\nabla^2\tilde{\omega}_i. \tag{2.8}$$

Combining (2.5), (2.7) and (2.8) we obtain

$$\frac{\mathrm{D}^{\tilde{u}}\omega_r}{\mathrm{D}^{\tilde{u}}t} = \omega_j s_{rj} + \frac{1}{Re}\left(\nabla^2\omega_r - \frac{\omega_r}{r^2} - \frac{2}{r^2}\frac{\partial\omega_\theta}{\partial\theta}\right) + \Omega_\theta s_{r\theta} + \omega_z S_{rz}, \tag{2.9}$$

$$\frac{\mathrm{D}^{\tilde{u}}\omega_\theta}{\mathrm{D}^{\tilde{u}}t} = \omega_j s_{\theta j} + \frac{1}{Re}\left(\nabla^2\omega_\theta - \frac{\omega_\theta}{r^2} + \frac{2}{r^2}\frac{\partial\omega_r}{\partial\theta}\right) + \Omega_\theta s_{\theta\theta} - u\frac{\partial\Omega_\theta}{\partial r} + \frac{u\Omega_\theta}{r}, \tag{2.10}$$

$$\frac{\mathrm{D}^{\tilde{u}}\omega_z}{\mathrm{D}^{\tilde{u}}t} = \omega_j s_{zj} + \frac{1}{Re}\nabla^2\omega_z + \Omega_\theta s_{z\theta} + \omega_r S_{rz} \tag{2.11}$$

and so

$$\begin{aligned}\frac{\mathrm{D}^{\tilde{u}}\omega^2/2}{\mathrm{D}^{\tilde{u}}t} = {}& \omega_i\omega_j s_{ij} + \frac{1}{Re}\left(\omega_i\nabla^2\omega_i - \frac{\omega_r^2}{r^2} - \frac{2\omega_r}{r^2}\frac{\partial\omega_\theta}{\partial\theta} - \frac{\omega_\theta^2}{r^2} + \frac{2\omega_\theta}{r^2}\frac{\partial\omega_r}{\partial\theta}\right)\\ & + \omega_r\Omega_\theta s_{r\theta} + \omega_r\omega_z S_{rz} + \omega_\theta\Omega_\theta s_{\theta\theta} + \omega_z\Omega_\theta s_{z\theta} + \omega_z\omega_r S_{rz}\\ & - u\omega_\theta\frac{\partial\Omega_\theta}{\partial r} + \frac{u\omega_\theta\Omega_\theta}{r}.\end{aligned} \tag{2.12}$$

It turns out that v_n consists of four components with distinct physical origin:

$$v_n = v^{inv} + v^{vis} + v^{it} + v^{vt}, \tag{2.13}$$

where v^{inv} is a nonlinear inertial term due to the self-amplifying nature of velocity derivatives,

$$v^{inv} = -\frac{2\omega_i\omega_j s_{ij}}{|\nabla\omega^2|}, \tag{2.14}$$

v^{vis} is a viscous term,

$$v^{vis} = -\frac{2Re^{-1}\left(\omega_i\nabla^2\omega_i - \dfrac{\omega_r^2}{r^2} - \dfrac{2\omega_r}{r^2}\dfrac{\partial\omega_\theta}{\partial\theta} - \dfrac{\omega_\theta^2}{r^2} + \dfrac{2\omega_\theta}{r^2}\dfrac{\partial\omega_r}{\partial\theta}\right)}{|\nabla\omega^2|}, \tag{2.15}$$

v^{it} is given by linear interactions between the gradient of the laminar velocity profile and gradients of the perturbation velocity,

$$v^{it} = -\frac{2(\omega_r\Omega_\theta s_{r\theta} + \omega_r\omega_z S_{rz} + \omega_\theta\Omega_\theta s_{\theta\theta} + \omega_z\Omega_\theta s_{z\theta} + \omega_z\omega_r S_{rz})}{|\nabla\omega^2|}, \tag{2.16}$$

and, finally, there is a term v^{vt} associated with radial transport of laminar vorticity,

$$v^{vt} = \frac{2u\omega_\theta\dfrac{\partial\Omega_\theta}{\partial r} - \dfrac{2u\omega_\theta\Omega_\theta}{r}}{|\nabla\omega^2|}. \tag{2.17}$$

3. Numerical implementation and resolution tests

The difficulty due to the coupling of pressure and solenoidal velocity field in the Navier–Stokes equation is resolved here by employing a toroidal–poloidal formulation,

https://doi.org/10.1017/jfm.2013.127 Published online by Cambridge University Press

where the velocity is written as $\tilde{\boldsymbol{u}} = \boldsymbol{\nabla} \times (\hat{\boldsymbol{z}}\psi) + \boldsymbol{\nabla} \times \boldsymbol{\nabla} \times (\hat{\boldsymbol{z}}\phi)$. Here ψ and ϕ are the toroidal and poloidal potentials, respectively. With this representation, the Navier–Stokes equations reduce to a set of linear systems of ψ and ϕ, which are solved with a hybrid spectral finite-difference method. In the radial direction, the explicit finite-difference method is used to calculate derivatives with respect to radial coordinate r. In the streamwise and azimuthal directions, the flow field is periodic, hence allowing a Fourier representation for the unknowns as follows:

$$A(r, \theta, z) = \sum_{k=-K}^{K} \sum_{m=-M}^{M} A_{km}(r) \exp(\mathrm{i}akz + \mathrm{i}m\theta), \tag{3.1}$$

where αk and m give streamwise and azimuthal wavenumbers, respectively. The influence-matrix technique is used to deal with the boundary conditions and the time step is dynamically controlled with the information from a Crank–Nicolson corrector step. For further details of the formulation, see Willis & Kerswell (2009).

The governing equation of vorticity $\tilde{\boldsymbol{\omega}} = \boldsymbol{\nabla} \times \tilde{\boldsymbol{u}}$ is obtained by simply taking the curl of the Navier–Stokes equations. In order to numerically evaluate all terms contributing to the propagation velocity of vorticity relative to the fluid (see § 2), the perturbation vorticity equations are written as follows:

$$\frac{\mathrm{D}^{\tilde{u}}\boldsymbol{\omega}}{\mathrm{D}^{\tilde{u}}t} = (\boldsymbol{\Omega} \cdot \boldsymbol{\nabla})\boldsymbol{u} + (\boldsymbol{\omega} \cdot \boldsymbol{\nabla})\boldsymbol{U} + (\boldsymbol{\omega} \cdot \boldsymbol{\nabla})\boldsymbol{u} - (\boldsymbol{u} \cdot \boldsymbol{\nabla})\boldsymbol{\Omega} + \frac{1}{Re}\Delta\boldsymbol{\omega}. \tag{3.2}$$

All propagation velocity components are calculated as defined in the previous section (equations (2.13)–(2.17)). Two points are worth mentioning here. First, the term $\partial\boldsymbol{\omega}/\partial t$ is calculated using the centred second-order finite-difference scheme. To be specific, starting from a flow field at time t, we perform time integration twice with a fixed and very small time step, arriving at time $t + 2\Delta t$. The term $\partial\boldsymbol{\omega}/\partial t$ at time instant $t + \Delta t$ is approximated by $(\boldsymbol{\omega}_{t+2\Delta t} - \boldsymbol{\omega}_t)/2\Delta t$, while all other terms are evaluated at time $t + \Delta t$. A time step of $\Delta t = 2.5 \times 10^{-6}\, D/U$ was found to be small enough to give a converged $\partial\boldsymbol{\omega}/\partial t$. Second, the term $\boldsymbol{u} \cdot \boldsymbol{\nabla}\boldsymbol{\omega}$ (also part of $\mathrm{D}^{\tilde{u}}\boldsymbol{\omega}/\mathrm{D}^{\tilde{u}}t$) is not evaluated directly but as $\boldsymbol{u} \cdot \boldsymbol{\nabla}\boldsymbol{\omega} = \boldsymbol{\nabla} \times (\boldsymbol{u} \cdot \boldsymbol{\nabla}\boldsymbol{u}) + \boldsymbol{\omega} \cdot \boldsymbol{\nabla}\boldsymbol{u}$, which is found to give much more accurate results. Note that here the solenoidality of velocity and vorticity has been taken into consideration.

3.1. *Numerical accuracy of the vorticity equation*

To ensure that all velocity components are calculated with sufficient accuracy, the numerical resolution and the balance between the two sides of the enstrophy equation (2.12) were tested. Here the balance is measured by the $L2$-norm, which is defined as

$$\|\epsilon\|_2 := \sqrt{\frac{\iiint |\mathrm{D}\omega^2/\mathrm{D}t - \mathrm{RHS}|^2 \, r \, \mathrm{d}r \, \mathrm{d}\theta \, \mathrm{d}z}{\iiint |\mathrm{RHS}|^2 \, r \, \mathrm{d}r \, \mathrm{d}\theta \, \mathrm{d}z}}, \tag{3.3}$$

where RHS is the right-hand side of (2.12), and the integration is carried out over the whole computational domain. The balance test was done in a simulation of a turbulent puff at $Re = 2200$ in a $16\pi D$-long pipe. Various resolutions and stencil widths were tested and, for each parameter combination, around 15–30 snapshots spaced by a time interval of $\sim 10D/U$ were studied.

https://doi.org/10.1017/jfm.2013.127 Published online by Cambridge University Press

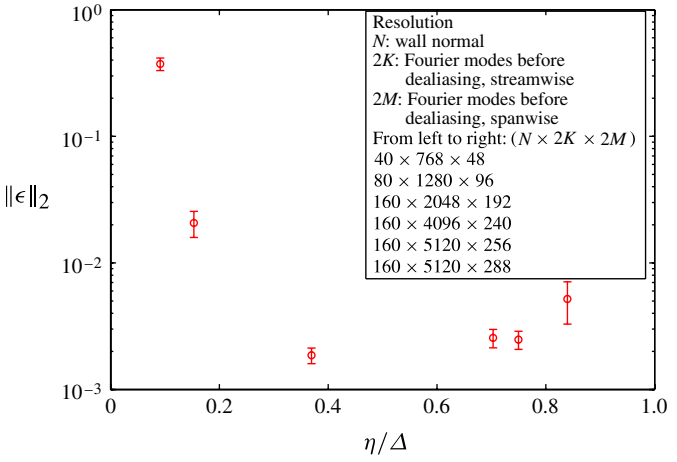


FIGURE 1. (Colour online) Time-averaged L2-norm $\|\epsilon\|_2$ for various resolutions tested. The abscissa shows the ratio between Kolmogorov scale η and grid spacing Δ, which is used here as a measure of resolution. The error bars display the standard deviation, and details of the resolutions are shown in the inset.

As shown in figure 1, the global norm of the balance $\|\epsilon\|_2$ decreases significantly with drastically increasing resolutions. The spatial resolution is represented here by the ratio between the smallest length scale of the flow, η, and the maximum grid spacing of the simulation, $\Delta = \max(\Delta_r, \Delta_\theta, \Delta_z)$. The smallest length scale is the Kolmogorov length scale defined as $\eta = (Re^3\varepsilon)^{1/4}$, where $\varepsilon = 2Re^{-1}\langle s_{ij}s_{ij}\rangle_{r,\theta}$ was evaluated at the downstream location where $\langle\omega^2\rangle_{r,\theta}$ has a maximum (angle brackets $\langle\cdot\rangle$ denote the average). However, the last four resolutions do not show much difference in balance, implying that, from the point of view of the balance of the enstrophy equation, these spatial resolutions are high enough. All points were obtained by taking the average of the norms over all the snapshots studied, as mentioned above. We note that the stencil width used in the radial finite-difference discretization also influences the balance; namely, a wider stencil yields more accurate radial derivatives but consumes more memory and computing time. Stencils with 9, 13 and 17 points were tested and finally a 13-point stencil was chosen for later analysis.

At this point it is worth remarking that an accurate balance of the vorticity equation does not necessarily imply that the simulations are resolved enough to compute interface propagation velocities at the instantaneous interface locations accurately using the method of § 2. The reason is that two additional processing steps are required for the analysis, namely, isosurfaces are computed using a standard routine in MATLAB based on the 'marching cubes' algorithm and the propagation velocity is then interpolated linearly in space from the grid points of the simulation to the isosurface locations.

3.2. *Mass-conservation check*

Mass conservation requires that the temporal change of the total volume of turbulent fluid V_t equals the volume flux $-Q$ across the level surface delimiting turbulent from

https://doi.org/10.1017/jfm.2013.127 Published online by Cambridge University Press

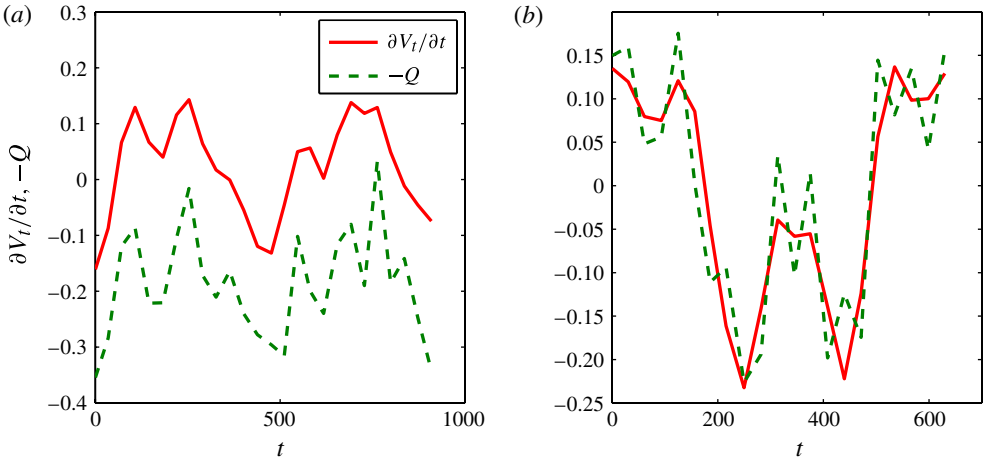


FIGURE 2. (Colour online) Terms of (3.4) as a function of time for (*a*) the lowest ($40 \times 768 \times 48$) and (*b*) the highest ($160 \times 5120 \times 288$) resolutions. The chosen isolevel is $c_{\omega^2}/\max\langle\omega^2\rangle_{r,\theta} = 10^{-2}$, for this and all following results below.

laminar flow regions, that is,

$$\frac{\partial V_t}{\partial t} = -\int_A v_n \,\mathrm{d}A = -Q, \tag{3.4}$$

where A is the area of the isosurface. The volume flux is taken with a minus sign in (3.4), because v_n is negative when the change of state is from laminar to turbulent (the surface normal $\hat{\boldsymbol{n}}$ points towards increasing ω^2). The quantity v_n was interpolated linearly in space to the centroids of the triangles that constitute the isosurface. The integral was calculated by summing the products between triangle area and v_n at its centroid. The temporal derivative $\partial V_t/\partial t$ was approximated using the second-order finite-difference scheme described in the previous subsection between the available snapshots. Since the temporal spacing considered between the snapshots is large ($\sim 10D/U$), we do not expect a very accurate pointwise correspondence between $\partial V_t/\partial t$ and $-Q$. However, statistically the balance must hold.

Figure 2 shows the time evolution of the left-hand side versus the right-hand side of (3.4) for (*a*) the lowest and (*b*) the highest resolutions tested. It can be seen that for the lowest-resolution case the volume flux is systematically lower than the temporal change of volume (figure 2*a*), indicating that this resolution is not sufficient to calculate the volume flux accurately. In contrast, for the highest-resolution case, the two curves are very close to each other (figure 2*b*). The time average of the terms of (3.4) is shown for all the resolutions tested in figure 3, where the error bars depict the 95 % confidence interval. For increasing resolution the two time-averaged terms of (3.4) approach each other and for the highest resolution tested the correspondence is very close (figure 3). With this we conclude that at the highest resolution ($160 \times 5120 \times 288$) interface velocities are accurately computed, and this is the resolution used for the results below. The data used consist of 90 snapshots from a simulation with duration of about $3000D/U$, where the example time series shown in this paper is based on the first 20 snapshots.

https://doi.org/10.1017/jfm.2013.127 Published online by Cambridge University Press

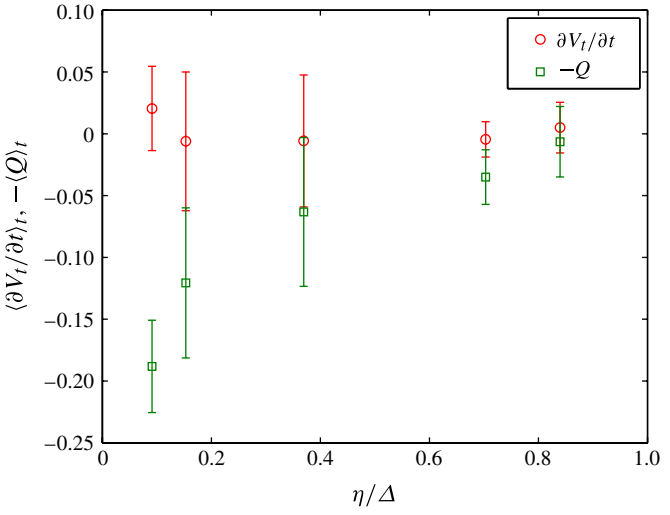


FIGURE 3. (Colour online) Average value of the two terms of (3.4) for the different resolutions tested. The resolution is represented by the ratio between Kolmogorov length scale η and grid spacing Δ. The error bars display the 95 % confidence interval.

4. Results

Figure 4(*a*) shows a snapshot of a puff at Reynolds number $Re = 2200$ displaying contours of the instantaneous enstrophy distribution in an (r, z) cross-section. The full length of the computational domain $32\pi R$ is displayed on the figure. There is a region where ω^2 has a relative maximum at about $z/R \simeq 20$, the location of the core of the puff, and one notes that the gradient of ω^2 is steeper upstream (trailing edge) than downstream (leading edge). Across the computational domain ω^2 varies over more than six orders of magnitude and the range of about 10^{-1}–10^{-4} constitutes an interval for the possible choice of an isolevel that discriminates between laminar and turbulent regions (i.e. the boundary of the puff). Levels above 10^{-1} select isolated patches of high vorticity in the core of the puff, and for levels below 10^{-4} the shape of the surface starts to be influenced by the finite size of the domain. The puff boundary as detected using an isolevel $c_{\omega^2}/\max\langle\omega^2\rangle_{r,\theta} = 10^{-2}$ and is shown in figure 4(*b*) as a binary image. There is a well-defined trailing edge interface and a more convoluted leading edge with incursions of laminar fluid deep into the structure (figure 4*b*).

Figure 4(*c*) displays the same binary image without fully entrapped laminar islands, showing that only a few small patches constitute laminar islands, while most laminar patches are connected to the outer laminar region. A three-dimensional view of the local propagation velocity v_n normalized by the Kolmogorov length scale $u_\eta = (\varepsilon/Re)^{1/4}$ is rendered over the isosurface for the same snapshot in figure 4(*d*). It can be seen that there are essentially two separate isosurfaces representing the trailing and leading interfaces of the puff, respectively. In between these two large surfaces, smaller disconnected patches can be identified. The trailing edge is shown in the bottom panel (figure 4*e*) from a side view (left) and from a $\pm 45°$ viewing angle around the radial axis (centre and right). The surface appears to be smoother where it faces the laminar region (figure 4*e*, centre), whereas it looks rather rough where it faces the turbulent region (figure 4*e*, right).

https://doi.org/10.1017/jfm.2013.127 Published online by Cambridge University Press

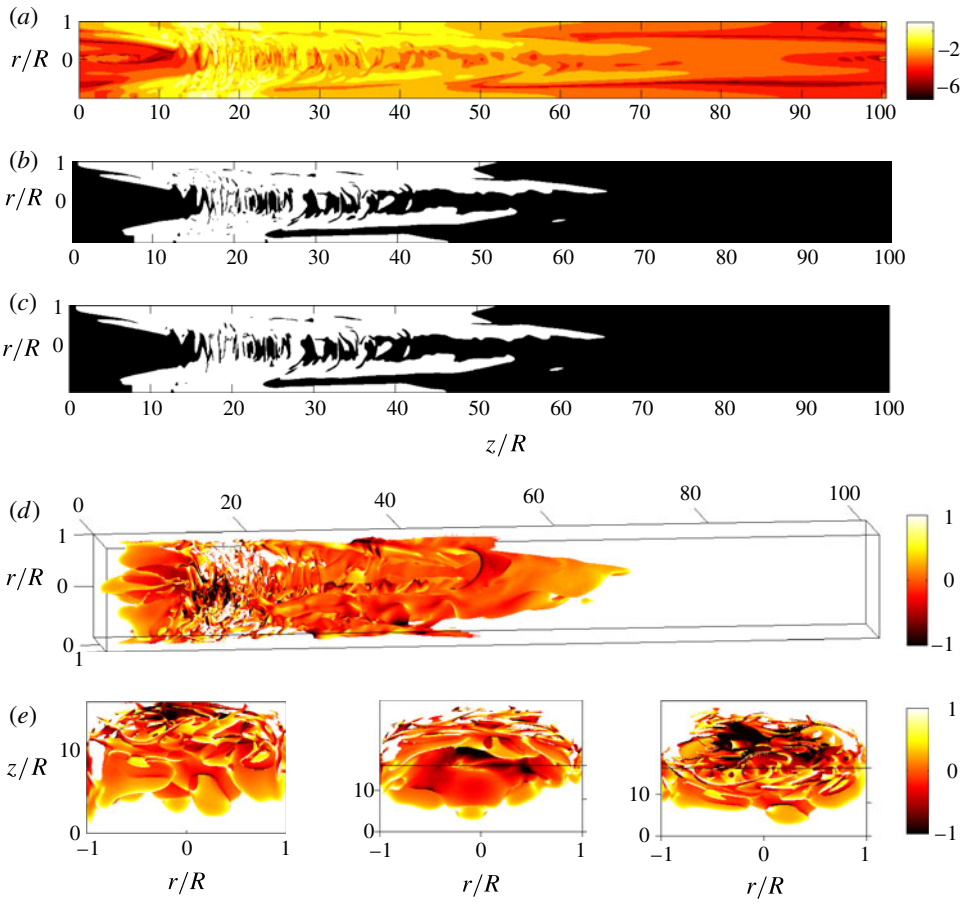


FIGURE 4. (Colour online) (*a*) Instantaneous enstrophy distribution $\omega^2/\max\langle\omega^2\rangle_{r,\theta}$ in a longitudinal slice of a turbulent puff at $Re = 2200$; the colour scale is logarithmic. (*b*) Binary image of all pixels where $\omega^2 > c_{\omega^2}$ with the chosen isovalue $c_{\omega^2}/\max\langle\omega^2\rangle_{r,\theta} = 10^{-2}$; and (*c*) the same binary image without disconnected laminar islands. (*d*) Three-dimensional view of the local propagation velocity v_n/u_η, where u_η is the Kolmogorov velocity, rendered over the isosurface with the chosen isovalue. There are essentially two separate surfaces; the first represents the trailing edge and the second the leading edge of the puff. (*e*) The trailing edge is shown from a side view (left) and from a $\pm 45°$ viewing angle around the radial axis (centre and right). For better visibility the view aspect ratio is quenched in the streamwise direction by a factor 6 (*a–d*) and 12 (*e*), respectively.

Figure 5 depicts the fluid volume of different flow regions as a function of the isolevel c_{ω^2}. The different regions are turbulent (V_t) ($\omega^2 > c_{\omega^2}$) and laminar (V_l) flow regions ($\omega^2 < c_{\omega^2}$), and turbulent (V_{ti}) and laminar (V_{li}) islands, respectively. As mentioned above, high isolevels ($c_{\omega^2}/\max\langle\omega^2\rangle_{r,\theta} \sim 1$) represent intense and fragmented vorticity regions in the core of the puff, which have a relatively small volume, comparable to the volume of disconnected turbulent islands (figure 5*a*). Conversely, very low isolevels ($c_{\omega^2}/\max\langle\omega^2\rangle_{r,\theta} \sim 10^{-5}$) select an envelope of the puff, where the volume of laminar fluid remaining in the domain becomes rather small. Outside the range $[10^{-4}, 10^{-1}]$ it is not possible any more to distinguish between two individual surfaces that are large and connected, i.e. the trailing and leading edges

https://doi.org/10.1017/jfm.2013.127 Published online by Cambridge University Press

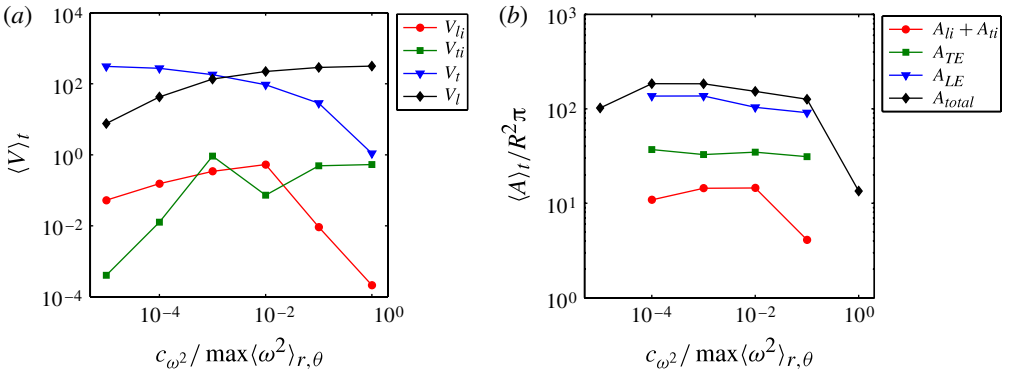


FIGURE 5. (Colour online) (*a*) Threshold dependence of the volume of turbulent islands V_{ti}, laminar islands V_{li}, turbulent volume V_t and laminar volume V_l in the domain, and (*b*) the area associated with disconnected islands A_{li+ti}, trailing edge A_{TE}, leading edge A_{LE} and total area A_{total}.

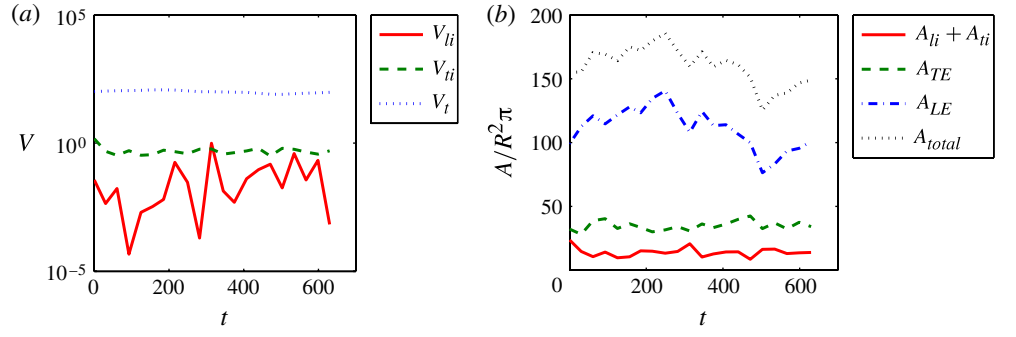


FIGURE 6. (Colour online) (*a*) Time evolution of the volume of turbulent islands V_{ti}, laminar islands V_{li} and total volume of the puff V_t, and (*b*) the area associated with disconnected islands A_{li+ti}, trailing edge A_{TE}, leading edge A_{LE} and total area A_{total}.

of the puff, whose areas are shown in figure 5(*b*). The area of the leading edge decreases somewhat with increasing isolevel, whereas the area of the trailing edge is less sensitive. As expected, the leading edge of the puff has the largest area, followed by the trailing edge and, finally, disconnected patches, which occupy about half the area of the trailing edge. Even though the volume of disconnected islands is typically small (figure 5*a*), their surface area is not negligible and may contribute up to about 10 % to the total surface area (figure 5*b*).

A time series of (*a*) the volumes and (*b*) the areas is plotted in figure 6 for the selected isolevel $c_{\omega^2}/\max\langle\omega^2\rangle_{r,\theta} = 10^{-2}$. For this isolevel, the volume occupied by laminar islands V_{li} is typically about two orders of magnitude smaller than V_t and the volume occupied by turbulent islands V_{ti} is more than three orders of magnitude smaller than V_t (figure 6*a*). Figure 6(*b*) shows that the area of the leading edge shows the strongest fluctuations, but when normalized by their means the time variations of all surface types are comparable to each other (not shown). It is well known that, owing to their strong convolution, interfaces possess a large area when

https://doi.org/10.1017/jfm.2013.127 Published online by Cambridge University Press

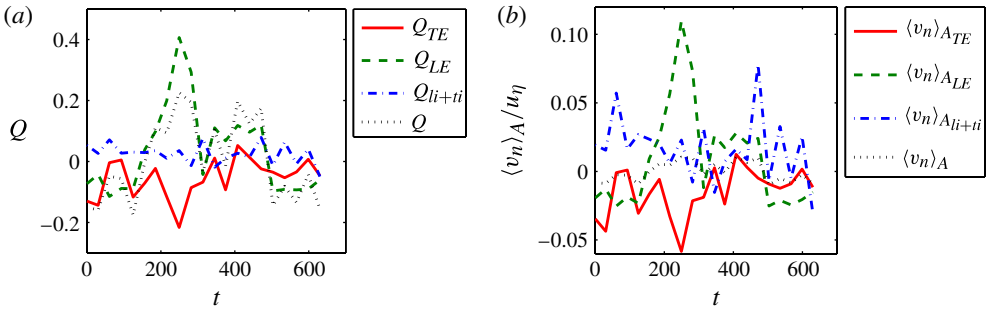


FIGURE 7. (Colour online) (*a*) Time evolution of the volume flux, and (*b*) local propagation velocity averaged over surface area and normalized by Kolmogorov velocity u_η for disconnected islands $li + ti$, trailing edge *TE* and leading edge *LE*.

compared to their projected area, i.e. the area projected on the axis of average propagation. For the present case of circular pipe flow, the axis of propagation is the streamwise direction and the projected area is the cross-sectional area of the pipe. However, the observed high ratios of order $O(10^2)$ (figure 6*b*) at the given moderate Reynolds number distinguish localized turbulence in transitional wall-bounded shear flows from the interfaces of turbulent free shear flows like turbulent jets (e.g. Catrakis & Dimotakis 1996; Wolf *et al.* 2012) or wakes (e.g. Bisset, Hunt & Rogers 2002), where, at comparable Reynolds number, the ratio between convoluted and projected area is significantly smaller, $A/A_{projected} < 10$. (It has been shown that for turbulent free shear flows the ratio between total and projected areas can be estimated assuming that the surface convolutions are of fractal geometry and the ratio is expressed as $A/A_{projected} = (\eta/L)^{2-d} \propto Re^{1/4}$, where L is the integral length scale of turbulence and $d = 7/3$ is the fractal dimension (e.g. Sreenivasan 1991).) As one possible reason for this difference we infer that, in addition to fluctuating strain rate, the laminar base flow may strongly stretch and amplify the area of the isosurface. Such a mean strain rate exists also for turbulent free shear flows, but in that case it is small compared to the strain rate of the turbulent eddies (e.g. Townsend 1966).

4.1. *Local and global propagation velocity*

The evolution of the volume flux across the isosurface with time is shown in figure 7(*a*) for trailing edge, leading edge and detached islands, respectively. The trailing edge is mostly characterized by a net transition from the laminar to the turbulent state ($Q < 0$), while the opposite is true for detached islands ($Q > 0$). At this Reynolds number $Re = 2200$, the leading edge fluctuates between positive and negative values, indicating that it is mostly the leading edge that is responsible for the great variability of the size of the puff over time. The magnitude of the volume flux contributed by detached islands is smaller than those of the trailing and leading edges in terms of both mean and variance. Over time, the positive volume fluxes of leading edge and detached islands balance the negative flux at the trailing edge so that the puff preserves its volume, i.e. on average it neither grows nor shrinks.

The volume flux divided by the surface area yields the local entrainment velocity averaged over the surface area, $\langle v_n\rangle_A$, shown in figure 7(*b*). Since the surface areas of the trailing and leading edges vary comparatively little over time, the trends of $\langle v_n\rangle_A$ are similar to the behaviour of the volume flux Q. The magnitudes of $\langle v_n\rangle_A$ are

https://doi.org/10.1017/jfm.2013.127 Published online by Cambridge University Press

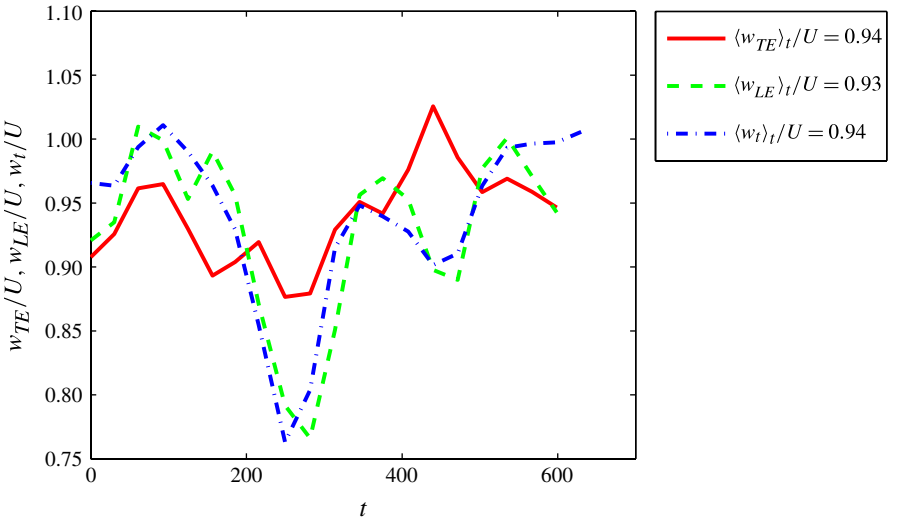


FIGURE 8. (Colour online) Propagation speed of the centre of mass of turbulent volume w_t, trailing edge w_{TE} and leading edge w_{LE}, respectively, normalized by the average flow velocity.

smaller than the Kolmogorov velocity u_η (figure 7*b*). For interfaces bounding vortical from irrotational flow regions, Corrsin & Kistler (1955) postulated that $v_n \propto u_\eta$, and Holzner & Lüthi (2011) found evidence for such a behaviour in a flow without mean shear. It seems that localized turbulence surrounded by laminar shear flow at the given moderate Re shows smaller mean values of v_n compared to a flow without mean shear (Holzner & Lüthi 2011).

We can calculate the propagation speed of the puff w_t from the displacement of the centre of mass of the turbulent volume over time and, similarly, we obtain the speed of the trailing edge w_{TE} and leading edge w_{LE} from the displacement of the centroid of the surface areas, respectively. The result is shown in figure 8, where the velocities are normalized by the average flow speed U. We find that at our Reynolds number $Re = 2200$ the puff propagates slightly slower than the mean flow speed, at $0.94U$, in excellent quantitative agreement with the experiments and simulations of Avila *et al.* (2011). Since the puff preserves its size, the average of the velocities of the centre of mass and of its interface are close to each other (see figure 8). The fact that the average flow is faster than the turbulent puff implies that laminar fluid must on average cross the turbulent region. The predominant entrainment at the trailing edge versus predominant relaminarization at the leading edge shown above is a plausible process that accounts for this behaviour. More fluid crosses the trailing edge from the laminar to the turbulent side than from turbulent to laminar, making the trailing edge slightly slower than the mean flow (its centroid moves towards the laminar side), whereas at the leading edge more fluid crosses the surface from the turbulent to the laminar side, making the surface again slightly slower than the mean flow (its centroid moves towards the turbulent side). Hence this is the process that determines the speed of the puff. With increasing Re we expect that the speed of the trailing edge becomes slower and the leading edge faster because of increased entrainment across both surfaces, i.e. for a slug much less fluid crosses the surface from the turbulent to the laminar side and accounts for the large speed. This is also reminiscent of the conclusions for the behaviour of slugs in Wygnanski & Champagne (1973).

https://doi.org/10.1017/jfm.2013.127 Published online by Cambridge University Press

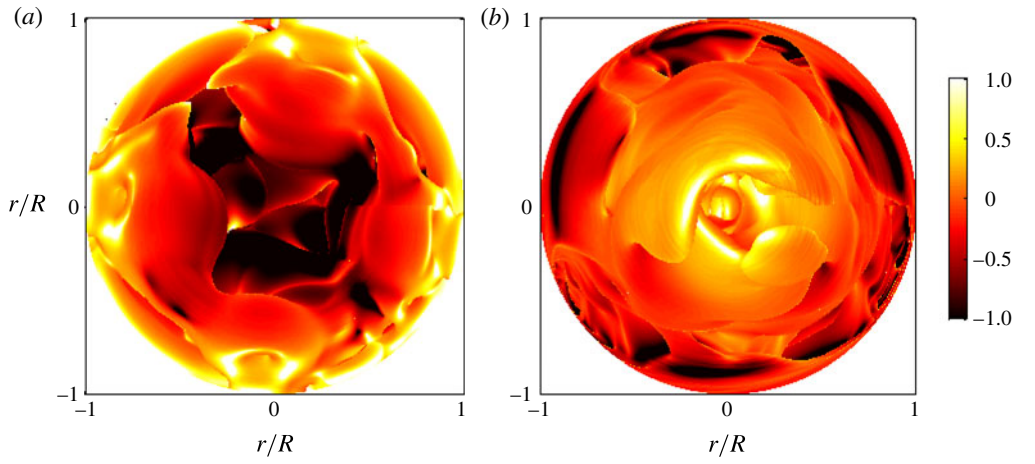


FIGURE 9. (Colour online) The local propagation velocity v_n rendered over the isosurface seen (*a*) from a viewpoint downstream (leading edge) and (*b*) from upstream (trailing edge) of the puff.

Since puffs are exposed not only to an average flow, but to a laminar flow profile, it is interesting to analyse the effects of transport by the laminar base flow versus mass transfer through the laminar–turbulent boundary more closely. The same rendering of figure 4(*e*) above is shown in figure 9 from a viewpoint downstream (leading edge, figure 9*a*) and upstream (trailing edge, figure 9*b*). We see that the local propagation velocity v_n can attain both positive and negative values at both the trailing and the leading interfaces. The main qualitative difference is that at the leading edge v_n is mostly positive in the centre, i.e. fluid relaminarizes, whereas it is mostly negative close to the wall, i.e. fluid is entrained and becomes turbulent (figure 9*a*). At the trailing edge it is the opposite, with v_n mostly negative in the centre, whereas it is mostly positive close to the wall (figure 9*b*). It appears, therefore, that the sign of v_n is such that it opposes the advection of the interfaces due to the laminar profile, which is slower than the average velocity at the wall and faster than the average in the bulk.

Figure 10 depicts (*a*) surface area, (*b*) local propagation velocity and (*c*)volume flux, conditionally averaged on the radial coordinate for the three surface types, trailing edge, leading edge and detached islands. The surface areas for the three surface types increase for increasing r, which essentially reflects the circular geometry of the pipe. Local extremal points can be brought into correspondence with a varying degree of folding qualitatively visible in figure 4. For example, at the leading edge there are deep incursions of laminar fluid in the centre and at the sides (figure 10*a*), which seem to be associated with the two relative maxima of the surface area at $r \simeq 0.2$ and 0.8, respectively. The magnitude of the local propagation velocity averaged over the surface is strongest in the centre (trailing edge), where it has a negative sign, and reaches positive values with maximum close to the wall (figure 10*b*). The magnitudes of $\langle v_n \rangle_A$ at the leading edge and detached islands are smaller compared to the trailing edge. The volume flux of trailing and leading edges shows an approximate symmetry about the axis $Q = 0$; the profile attains a relative maximum (minimum) for the leading edge (trailing edge) at $r \simeq 0.5$ and changes sign at $r \simeq 0.7$, which is approximately the radial location where the laminar profile matches the mean flow velocity (figure 10*c*). The volume flux associated with detached islands remains comparatively small and

https://doi.org/10.1017/jfm.2013.127 Published online by Cambridge University Press

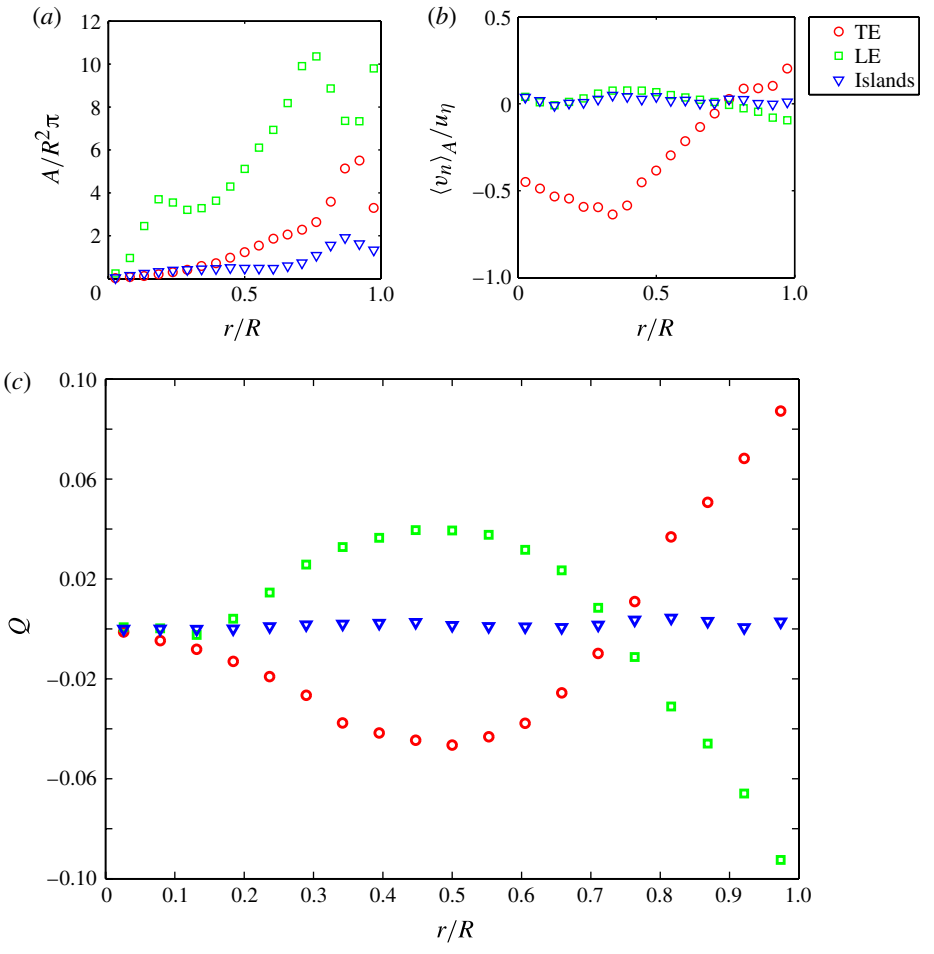


FIGURE 10. (Colour online) (*a*) Surface area, (*b*) local propagation velocity and (*c*) volume flux conditionally averaged on the radial coordinate for the three surface types, trailing edge (○), leading edge (□) and detached islands (▽).

shows only a weak dependence on the radial coordinate. The trends of figure 10(*c*) at the trailing and leading edges are consistent with the qualitative result of figure 9 and show that fluxes across the two puff interfaces almost balance and allow the puff to preserve its shape. *A priori* one would not necessarily expect that there is a connection between volume flux associated with v_n and convective fluxes due to the fluid velocity. We can further examine this connection by invoking the mass balance introduced above (equation (3.4)) for a cylindrical slice of the puff.

4.2. *Mass balance in the co-moving frame of the turbulent puff*

Let us consider a slice of the cylindrical domain of thickness dz and ΔV_t^i denotes the turbulent volume contained in it. Mass conservation requires that the temporal change of turbulent volume in the slice equals the sum of convective transport of turbulent fluid across the two cross-sectional boundaries of the slice and the volume flux across the isosurface contained in the slice. It is more natural to consider this balance in the frame of reference moving with the velocity of the centroid of the turbulent volume w_t,

https://doi.org/10.1017/jfm.2013.127 Published online by Cambridge University Press

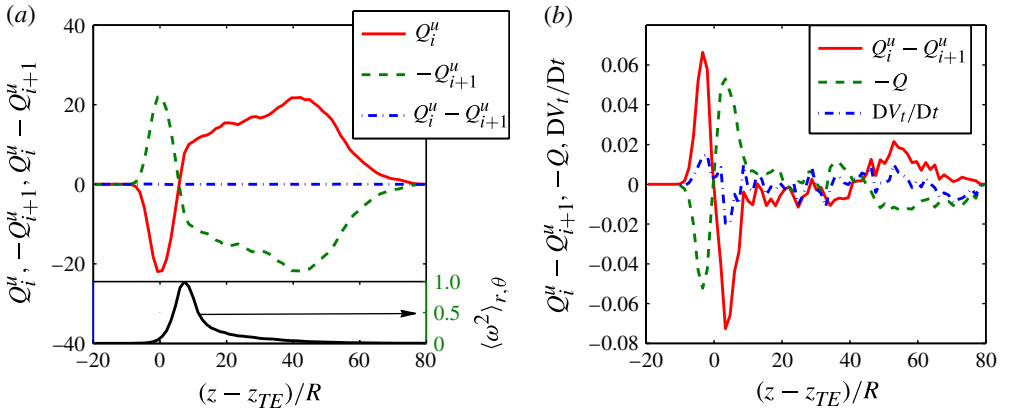


FIGURE 11. (Colour online) (*a*) The first two terms on the right-hand side of (4.1) and their sum, the enstrophy $\langle\omega^2\rangle_{r,\theta}$ normalized by its maximum (bottom), and (*b*) all terms of (4.1) in the co-moving frame of the puff. The streamwise coordinate z is centred at the centroid of the trailing edge.

and the local time derivative hence becomes a total derivative $\mathrm{D}^{w_t}/\mathrm{D}t$. The balance is written as

$$\begin{aligned}\frac{D^{w_t}\Delta V_t^i(t)}{\mathrm{D}t} = &\int_0^R\int_0^{2\pi} I(r,\theta,z_i,t)[\tilde{w}(r,\theta,z_i,t) - w_t(t)]r\,\mathrm{d}r\,\mathrm{d}\theta \\ &- \int_0^R\int_0^{2\pi} I(r,\theta,z_i+\mathrm{d}z,t)[\tilde{w}(r,\theta,z_i+\mathrm{d}z,t) - w_t(t)]r\,\mathrm{d}r\,\mathrm{d}\theta \\ &- \int_{A|_{z_i<z<z_i+\mathrm{d}z}} v_n\,\mathrm{d}A, \end{aligned} \tag{4.1}$$

where the first and second terms on the right-hand side are volume fluxes due to convective transport, Q_i^u at z_i and Q_{i+1}^u at $z_i + \mathrm{d}z$, respectively, the third term is the volume flux across the level surface and I is the intermittency function defined as

$$I = \begin{cases} 1 & \omega^2 \geqslant \text{isolevel}, \\ 0 & \omega^2 < \text{isolevel}. \end{cases} \tag{4.2}$$

Note that (3.4) above is easily recovered from (4.1) by summing all slices that constitute the turbulent volume, $V_t = \sum_1^{N_z} \Delta V_t^i$, given that for neighbouring slices the convective transport terms cancel each other out. A similar analysis in terms of variables conditioned on the intermittency function was considered in Dopazo (1977).

The first two terms on the right-hand side of (4.1) and their sum are shown in figure 11. The sign of the advective flux Q^u displays its direction; it is positive (negative) when the flux points in the downstream (upstream) direction, respectively. At the trailing edge the advective transport points upstream ($Q^u < 0$ for $z - z_{TE} \leqslant 6$), see figure 11(*a*), where the horizontal axis is centred at the centroid of the trailing edge. It points downstream ($Q^u > 0$) correspondingly at the leading edge. The two extremal points are approximately located at the centroids of the trailing edge (minimum) and leading edge (maximum), respectively. The change of sign occurs roughly at the point where the enstrophy is maximal, in the core of the puff

https://doi.org/10.1017/jfm.2013.127 Published online by Cambridge University Press

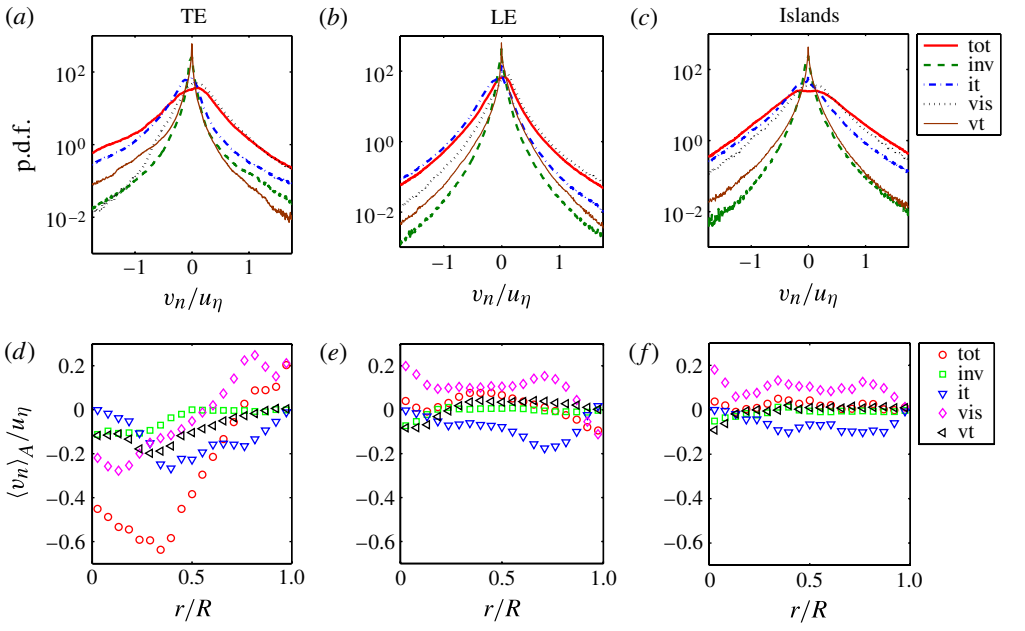


FIGURE 12. (Colour online) (*a–c*) The p.d.f.s and (*d–f*) the conditional averages on the radial coordinate of the components of v_n (equations (2.13)–(2.17)) for the three surface types, (*a,d*) trailing edge, (*b,e*) leading edge and (*c,f*) detached islands.

(figure 11*a*, bottom). This implies that there is a net transport of vortical fluid away from the core of the puff, consistent with the observations in Wygnanski *et al.* (1975) and Hof *et al.* (2010). For each slice the convective fluxes across the cross-sectional boundaries are very close to each other so that they almost cancel each other out (figure 11). The full balance of (4.1) is shown in figure 11(*b*). Advective fluxes contribute to a gain of vortical fluid in the rear end of the trailing edge ($Q_i^u - Q_{i+1}^u > 0$), which is the region close to the walls, and to a loss in the front end ($Q_i^u - Q_{i+1}^u > 0$), the region in the centre of the pipe. The situation is the opposite at the leading edge, where advective transport contributes to a loss of turbulent fluid on the upstream side (close to the walls), and to a gain on the downstream side (in the central region), respectively (figure 11*b*). The zero crossings are approximately located at the centroids of the trailing edge and the leading edge, respectively. The volume flux across the isosurface $-Q$ shows the opposite behaviour, so that there is an approximate balance of the three terms on the right-hand side of (4.1) and the change of volume is small everywhere along the axis of the pipe.

4.3. *Components of the local propagation velocity* v_n

Finally, we focus on the decomposition of the local propagation velocity (equations (2.13)–(2.17)). The probability density functions (p.d.f.s) of the components of v_n are depicted in figure 12(*a–c*) for the three surface types, (*a*) trailing edge, (*b*) leading edge and (*c*) detached islands. All distributions show tails that are heavier than a Gaussian distribution. Nevertheless, an interval of only a few Kolmogorov velocities is sufficient to comprise at least two decades of the p.d.f.s (figure 12*a–c*). The viscous term v_n^{vis} is positively skewed, as it contributes mostly to the destruction of enstrophy and hence to relaminarization. The linear term v_n^{it} due to interactions

https://doi.org/10.1017/jfm.2013.127 Published online by Cambridge University Press

between fluctuating vorticity and the gradient of the laminar velocity profile shows a negative skewness, i.e. it is the main contributor to the build-up of vorticity. The remaining two terms v_n^{inv} and v_n^{vt} are concentrated at comparatively lower magnitudes. The term v_n^{vt} associated with radial transport of laminar vorticity shows a strong negative skewness at the trailing edge, contributing to the build-up of vorticity, whereas it is more symmetric at the leading edge and detached islands.

Figure 12(*d–f*) shows the components of v_n conditionally averaged on the radial coordinate for the three surface types, (*d*) trailing edge, (*e*) leading edge and (*f*) detached islands. At the trailing edge, around the pipe centre, local transition to turbulence is brought about mostly by the viscous term by diffusion of vorticity and to some degree by the inviscid nonlinear term v_n^{inv} and the radial transport term v_n^{vt} (figure 12*d*). This is reminiscent of the results in Holzner & Lüthi (2011), who found a dominance of the viscous term ($v_n^{vis} < 0$) for a flow with no mean shear. For increasing r the linear term $v_n^{it} < 0$ dominates, while the viscous term changes sign and becomes positive ($v_n^{vis} > 0$, i.e. vorticity is destroyed via dissipation). Close to the wall, relaminarization is entirely dominated by viscous effects. At the leading edge, on average v_n^{vis} dominates the sign of v_n (figure 12*e*). For small r, $v_n^{vis} > 0$ is opposed by $v_n^{inv} < 0$ and $v_n^{vt} < 0$, whereas for larger r there is mostly a competition between the viscous term and v_n^{it}. Close to the wall, the viscous term changes sign ($v_n^{vis} < 0$) and brings about the local transition to turbulence. The average behaviour of detached islands (figure 12*f*) is to a large extent similar to the trends for the leading edge, except that the viscous term does not change sign close to the wall and the average v_n is mostly positive.

5. Discussion

One of the most important ingredients to improve our understanding of transition to turbulence in shear flows is to clarify how localized turbulence expands or decays and how bounding interfaces are maintained. In the past, many studies have focused on this aspect; however, they remain to some extent qualitative. The framework shown in this paper is a quantitative tool that allows one to assess in a direct way the physics of laminar–turbulent interfaces and how they spread and contaminate laminar flow. It is worth noting that for this analysis a substantially larger resolution is required than is necessary to compute converged puff speed, lifetime and splitting statistics (e.g. Willis & Kerswell 2007; Avila *et al.* 2010, 2011).

The main features of the method can be summarized as follows. First, the approach disentangles effects due to motion of the interface relative to the fluid (equation (2.4)) and the advective transport due to the fluid velocity. Second, it quantifies the growth of turbulent regions by considering the volume flux across the interface (equation (3.4)), involving local relative velocity and surface area. Third, it allows one to distinguish between linear contributions originating from the laminar base flow, nonlinear and viscous effects (equations (2.13)–(2.17)).

We have shown in this paper that the bounding edges of a turbulent puff propagate mostly through outward and inward motion of continuous surfaces that propagate relative to the fluid velocity. At the same time they are advected by the flow and stretched out by (i) the straining of large eddies and (ii) the laminar velocity profile, resulting in very large surface areas. In addition to the continuous propagation mechanism relative to the fluid, surface parts may locally detach, giving rise to small disconnected blobs of laminar fluid enclosed in the puff and patches of turbulent fluid

https://doi.org/10.1017/jfm.2013.127 Published online by Cambridge University Press

disconnected from the puff. The former are expected to play the key role in the splitting process (Avila *et al.* 2011).

5.1. *Local transition scenarios*

Our analysis shows that at the trailing edge local transition to turbulence occurs in the inner region, where turbulence is more vigorous, whereas fluid relaminarizes near the wall. This is largely consistent with previous results in the literature (e.g. Wygnanski *et al.* 1975; Bandyopadhyay 1986; Darbyshire & Mullin 1995; van Doorne & Westerweel 2009; Shimizu & Kida 2009; Duguet, Willis & Kerswell 2010), which described a roll-up of vortex layers that energize the puff at its trailing edge. Notably, we find that local transition at the trailing edge is mostly associated with linear stretching of vorticity due to the mean profile, and to some degree by radial transport of laminar vorticity, in the region where such a roll-up of vortex layers was observed ($0.3 < r/R < 0.7$), whereas nonlinear $\langle v_n^{inv} \rangle < 0$ and, more strongly, viscous effects $\langle v_n^{vis} \rangle < 0$ become appreciable in the core ($r/R < 0.3$) where these layers are strongly folded (figure 12*d*). Since the surface area is small in the core, in terms of volume flux, linear effects dominate the local transition at the trailing edge (figure 7*a*). The linear effects associated with the mean velocity profile and the rather elongated and smooth shape of the trailing edge in the roll-up region (figure 4) are reminiscent of the initial stage in the entrainment hypothesis of Townsend (1966), which is the formation of larger eddies that extract their energy from the mean shear and create surface area across which transfer of vorticity can take place.

The observation of small disconnected patches of laminar fluid in the interior of the puff raises the question of their dynamical significance. In particular, again the sequential entrainment picture, the one of engulfment, followed by stirring and molecular mixing, comes to mind (e.g. Townsend 1966). Our results suggest that this sequence of events cannot be a dominant process, since the volume flux associated with disconnected islands is positive in the mean, i.e. laminar blobs tend to expand and possibly may even reconnect to the boundaries. Also, in terms of magnitude of the volume flux, disconnected islands contribute less to the change of turbulent volume both in the mean and in terms of variance (figure 7*a*). This implies that the propagation of the puff is mostly determined by a continuous outward spreading of continuous surfaces that move relative to the fluid. However, it is important to note that previous investigations have highlighted the significance of puff splitting for the nucleation of new turbulent regions (Wygnanski *et al.* 1975; Darbyshire & Mullin 1995; van Doorne & Westerweel 2009; Avila *et al.* 2011). While the case under study here does not include such events, it would involve precisely the study of a laminar island that grows to a dimension large enough to reorganize and split a single turbulent structure into two parts.

We have shown that, in contrast to the trailing edge, at the leading edge relaminarization occurs in the central region and fluid is entrained viscously at the walls. Although an observation of entrainment through the leading edge near the wall was made by Wygnanski & Champagne (1973), these authors argued that it only occurs in turbulent slugs, i.e. at larger Reynolds number. Our results show that entrainment does occur at the leading edge for puffs as well and hence suggest that there are qualitative similarities between the dynamics of puffs and slugs not only as far as the trailing edge is concerned. This discrepancy is attributed here to difficulties in the early experimental studies of Wygnanski & Champagne (1973) and Wygnanski *et al.* (1975) to detect the leading front of a puff, because it is less sharp.

https://doi.org/10.1017/jfm.2013.127 Published online by Cambridge University Press

For the considered Reynolds number $Re = 2200$, the turbulent region on average neither grows nor shrinks. (At least at the time scales of $O(3000D/U)$ considered here – note that for times of $O(10^4 D/U)$ the puff will probably split into two at the given Reynolds number (Avila *et al.* 2011).) Given that, we showed that there is an equilibrium between the predominant local transition to turbulence at the trailing edge and predominant local relaminarization at the leading edge. This also implies that there must be a net transport of vortical fluid from the rear towards the front of the puff. Indeed, it turned out that convective fluxes redistribute vortical fluid in a non-trivial way. They augment the volume of turbulent fluid at the rear of the puff close to the walls and deplete it in the central region, while for the front part of the puff it is the other way round, i.e. convective fluxes deplete vortical fluid close to the wall and augment it in the centre (figure 11*b*). Volume fluxes due to the relative propagation velocity approximately balance these advective fluxes along the streamwise extent of the puff so that the change of turbulent volume is small everywhere. Finally, volumetric fluxes across the leading and trailing edges were found to show the same radial profile but opposite sign, and it is this approximate balance that allows the puff to preserve its characteristic shape.

5.2. *Comparison to turbulence interfaces bounded by an irrotational stream*

Compared to an interface bounded by an irrotational stream, the transitional flow considered herein has a large mean velocity gradient across the interface. One consequence is that, compared to turbulent flows with weak (e.g. jets, wakes) or no mean gradient (e.g. developing oscillating grid turbulence), the interface area is stretched out by a strong mean strain in addition to fluctuating stresses. This is a possible explanation for the observation of the larger surface areas (figure 6*b*) compared to free shear flows. On the other hand, the magnitude of v_n seems to be lower compared to measurements in a flow without mean shear or at the boundary of a round jet (Holzner & Lüthi 2011; Wolf *et al.* 2012 measured $\langle v_n \rangle_A \sim u_\eta$), except at the centre of the trailing edge (figure 12*d*). Nevertheless, similar to free shear flows, surface area and local propagation velocity adjust themselves such that the global propagation speed is a function of the flow rate only, i.e. it does not depend on viscosity or the fine scale details of the flow.

As inferred by Corrsin & Kistler (1955), the presence of laminar vorticity adds additional mechanisms to the viscous transfer of vorticity across the turbulence interface. These have been identified here as radial transport of laminar vorticity and linear stretching of fluctuating vorticity due to the gradient of the laminar velocity profile.

6. Conclusions and perspectives

In this study we have applied a Lagrangian approach to the laminar–turbulent interface of a turbulent puff in pipe flow. The method has highlighted the role of continuous relative motion of large convoluted surfaces for the dynamics of a turbulent puff. With growing computer power, the method may be applied at higher Reynolds number and shed light on the differences between puffs and slugs. It is expected that at higher *Re* the leading edge will be mostly entraining fluid and propagate faster. This could be due to changes of the surface topology, the physics of the local propagation velocity, a reorganization of advective fluxes in the interior of the structure, or changes in dynamics of surfaces (e.g. dis- and reconnections of surface parts). Finally, it would further be interesting to study the physics of puff splitting and puff decay using our

https://doi.org/10.1017/jfm.2013.127 Published online by Cambridge University Press

Lagrangian approach. As our method allows us to keep track of different parts of the bounding surfaces and their evolution, it has potential to bring new insights into the local dynamics of puff splitting and puff decay and relate their statistics to the propagation velocity of puffs.

Acknowledgements

M.H. acknowledges financial support from the Swiss National Science Foundation (SNF) under grant number PBEZP2-127831 and from the European Commission under the Marie Curie Intra-European Fellowship, project number 272886. S.B. acknowledges financial support from the Chinese State Scholarship Fund under grant number 2010629145. We thank A. P. Willis for sharing his hybrid spectral finite-difference code. Support from the Max Planck Society is acknowledged. We acknowledge computing resources from GWDG (Gesellschaft für wissenschaftliche Datenverarbeitung Göttingen) and the Jülich Supercomputing Centre (grant HGU16), where the simulations and analysis were performed.

REFERENCES

AVILA, K., MOXEY, D., DE LOZAR, A., AVILA, M., BARKLEY, D. & HOF, B. 2011 The onset of turbulence in pipe flow. *Science* **333** (6039), 192–196.

AVILA, M., WILLIS, A. P. & HOF, B. 2010 On the transient nature of localized pipe flow turbulence. *J. Fluid Mech.* **646**, 127–136.

BANDYOPADHYAY, P. R. 1986 Aspects of the equilibrium puff in transitional pipe flow. *J. Fluid Mech.* **163**, 439–458.

BISSET, D. K., HUNT, J. C. R. & ROGERS, M. M. 2002 The turbulent/non-turbulent interface bounding a far wake. *J. Fluid Mech.* **451**, 382–410.

CATRAKIS, H. J. & DIMOTAKIS, P. E. 1996 Mixing in turbulent jets: scalar measures and isosurface geometry. *J. Fluid Mech.* **317**, 369–406.

CORRSIN, S. & KISTLER, A. L. 1955 The free stream boundaries of turbulent flows. NACA Tech. Rep. TN-3133, TR-1244.

DARBYSHIRE, A. G. & MULLIN, T. 1995 Transition to turbulence in constant-mass-flux pipe flow. *J. Fluid Mech.* **289**, 83–114.

VAN DOORNE, C. W. H. & WESTERWEEL, J. 2009 The flow structure of a puff. *Phil. Trans. R. Soc.* A **367**, 489.

DOPAZO, C. 1977 On conditioned averages for intermittent turbulent flows. *J. Fluid Mech.* **81**, 433–438.

DUGUET, Y., WILLIS, A. P. & KERSWELL, R. R. 2010 Slug genesis in cylindrical pipe flow. *J. Fluid Mech.* **663**, 180–208.

HOF, B., DE LOZAR, A., AVILA, M., TU, X. & SCHNEIDER, T. 2010 Eliminating turbulence in spatially intermittent flows. *Science* **327**, 1491–1494.

HOF, B., DE LOZAR, A., KUIK, D. J. & WESTERWEEL, J. 2008 Repeller or attractor? Selecting the dynamical model for the onset of turbulence in pipe flow. *Phys. Rev. Lett.* **101** (21), 214501.

HOF, B., WESTERWEEL, J., SCHNEIDER, T. M. & ECKHARDT, B. 2006 Finite lifetime of turbulence in shear flows. *Nature* **443** (7107), 59–62.

HOLZNER, M., AVILA, A., DE LOZAR, A. & HOF, B. 2011 Lagrangian approach to turbulent puffs in pipe flow. *J. Phys. Conf. Ser.* **318**, 052031 (European Turbulence Conference, ETC 13).

HOLZNER, M., LIBERZON, A., NIKITIN, N., LÜTHI, B., KINZELBACH, W. & TSINOBER, A. 2008 A Lagrangian investigation of the small scale features of turbulent entrainment through particle tracking and direct numerical simulation. *J. Fluid Mech.* **598**, 465–475.

HOLZNER, M. & LÜTHI, B. 2011 Laminar superlayer at the turbulence boundary. *Phys. Rev. Lett.* **106**, 134503.

LINDGREN, E. R. 1969 Propagation velocity of turbulent slugs and streaks in transition pipe flow. *Phys. Fluids* **12** (2), 418–425.

https://doi.org/10.1017/jfm.2013.127 Published online by Cambridge University Press

MOXEY, D. & BARKLEY, D. 2010 Distinct large-scale turbulent–laminar states in transitional pipe flow. *Proc. Natl Acad. Sci. USA* **107** (18), 8091–8096.

ROTTA, J. 1956 Experimenteller Beitrag zur Entstehung turbulenter Strömung im Rohr. *Ing.-Arch.* **24**, 258–281.

SHAN, H., MA, B., ZHANG, Z. & NIEWSTADT, F. T. M. 1999 Direct numerical simulation of a puff and a slug in transitional cylindrical pipe flow. *J. Fluid Mech.* **387**, 39–60.

SHIMIZU, M. & KIDA, S. 2009 A driving mechanism of a turbulent puff in pipe flow. *Fluid Dyn. Res.* **41**, 045501.

SREENIVASAN, K. R. 1991 Fractals and multifractals in fluid turbulence. *Annu. Rev. Fluid Mech.* **23**, 539–604.

TOWNSEND, A. A. 1966 The mechanism of entrainment in free turbulent flows. *J. Fluid Mech.* **26**, 689–715.

WILLIS, A. P. & KERSWELL, R. R. 2007 Critical behavior in the relaminarization of localized turbulence in pipe flow. *Phys. Rev. Lett.* **98** (1), 014501.

WILLIS, A. P. & KERSWELL, R. R. 2009 Turbulent dynamics of pipe flow captured in a reduced model: puff relaminarization and localized edge states. *J. Fluid Mech.* **619**, 213–233.

WOLF, M., LÜTHI, B., HOLZNER, M., KRUG, D., KINZELBACH, W. & TSINOBER, A. 2012 Investigations on the local entrainment velocity in a turbulent jet. *Phys. Fluids* **24**, 105110.

WYGNANSKI, I. J. & CHAMPAGNE, F. H. 1973 On transition in a pipe. Part 1. The origin of puffs and slugs and the flow in a turbulent slug. *J. Fluid Mech.* **59**, 281–335.

WYGNANSKI, I. J., SOKOLOV, M. & FRIEDMAN, D. 1975 On transition in a pipe. Part 2. The equilibrium puff. *J. Fluid Mech.* **69**, 283–304.

https://doi.org/10.1017/jfm.2013.127 Published online by Cambridge University Press